

OPEN ACCESS

EDITED BY

Shuqing Zhang,
Tsinghua University, China

REVIEWED BY

Ying Wang,
Southeast University, China
Jianhang Zhu,
Huazhong University of Science and
Technology, China
Chenxi Hu,
The University of Hong Kong, Hong
Kong SAR, China

*CORRESPONDENCE

Chao Lu,
✉ lc_sgccsh@126.com

RECEIVED 09 October 2025

REVISED 13 November 2025

ACCEPTED 28 November 2025

PUBLISHED 12 January 2026

CITATION

Lu Y, Lu C, Lan S, Dai J and Ma Y (2026)
Operational risk assessment and energy
storage optimization for low-voltage
distribution networks based on DeepAR-KAN.
Front. Energy Res. 13:1721368.
doi: 10.3389/fenrg.2025.1721368

COPYRIGHT

© 2026 Lu, Lu, Lan, Dai and Ma. This is an
open-access article distributed under the
terms of the [Creative Commons Attribution
License \(CC BY\)](https://creativecommons.org/licenses/by/4.0/). The use, distribution or
reproduction in other forums is permitted,
provided the original author(s) and the
copyright owner(s) are credited and that the
original publication in this journal is cited, in
accordance with accepted academic practice.
No use, distribution or reproduction is
permitted which does not comply with
these terms.

Operational risk assessment and energy storage optimization for low-voltage distribution networks based on DeepAR-KAN

Yu Lu, Chao Lu*, Senlin Lan, Jiejie Dai and Yuan Ma

State Grid Shanghai Municipal Electric Power Company, Shanghai, China

Introduction: The operational environment of low-voltage distribution networks is becoming increasingly complex due to the high penetration of distributed energy resources and the growing diversity of end-user loads. Consequently, operational risks such as voltage deviations, three-phase unbalances, and active power overloads are becoming more prominent, posing serious challenges to power supply reliability and power quality.

Methods: To address these issues, this paper develops an integrated analytical and decision-making framework that unifies ultra-short-term probabilistic load forecasting, dynamic risk assessment, and energy storage optimization operations. First, an improved DeepAR-based probabilistic forecasting model is proposed, where the Kolmogorov–Arnold Network (KAN) is embedded to enhance the model's capacity for capturing complex nonlinear and stochastic features, improving short-term load forecasting accuracy. Second, a dynamic multi-risk assessment framework is constructed, which simultaneously evaluates voltage deviations, phase unbalances, and active power overload risks, and introduces time-decay weighting factors to achieve multi-time-step risk aggregation. Finally, an energy storage optimization model was formulated with the objective of minimizing the comprehensive operational risk, enabling proactive and risk-aware control of distribution network states.

Results: Case studies conducted on the IEEE 13-bus distribution system and practical data from a low-voltage distribution network demonstrated that the proposed framework enhances the situational awareness, dynamic adaptability, and proactive control capability of distribution systems against multi-dimensional operational risks.

Discussion: The results provide both theoretical insights and engineering references for improving the secure and resilient operation of future low-voltage distribution networks.

KEYWORDS

ultra-short-term load forecasting, risk assessment, energy storage optimization, low-voltage distribution network, DeepAR, three-phase unbalance

1 Introduction

With the rapid increasing of distributed photovoltaic (PV) generation and electric vehicle (EV) charging facilities in low-voltage distribution networks, system operation is facing unprecedented challenges (Deb et al., 2018). Issues such as voltage deviations

(Prakash et al., 2022), three-phase unbalances (Cao et al., 2024), and transformer overloading have become increasingly severe, directly constraining the power supply capacity and degrading the power quality of low-voltage networks. Against this backdrop, refined operational risk assessment has become crucial. Subsequently, the energy storage system (ESS), with its fast and flexible active/reactive power regulation capabilities, has emerged as a key solution for mitigating these multi-faceted risks (Li et al., 2023).

To effectively manage these emerging operational risks, the establishment of scientific and data-driven risk assessment methodologies is essential. Existing studies on power system risk assessment can be broadly divided into analytical and simulation-based approaches (Bie et al., 2024). Analytical methods assess operational risks through probabilistic modeling of uncertainties and the application of probabilistic power flow (PPF) calculations (He et al., 2019), offering high computational efficiency. For example (Lin et al., 2023), presents a systematic probabilistic power flow framework for static operational risk evaluation. Separately (Chen et al., 2025), integrates PPF with branch flow analysis to assess voltage fluctuation risk and guide optimal operation. However, analytical methods typically require complex derivations and are less effective in capturing high-dimensional nonlinear dynamics (Villanueva et al., 2014).

In contrast, simulation-based approaches utilize random sampling to emulate diverse operating conditions and estimate the probability distributions of risk indicators through repeated Monte Carlo trials. Although computationally intensive, they demonstrate superior adaptability and accuracy when addressing complex system behavior (Zhou et al., 2018). Such methods have been widely adopted in the risk (Zheng et al., 2020) and reliability assessment (Wang et al., 2024) of distribution networks. Building upon this foundation, the present study adopts a simulation-based framework to statistically estimate the occurrence probabilities of multiple risk indicators under various operating scenarios. Furthermore, time-decay weighting is incorporated to capture the temporal evolution of risks and aggregate dynamic risk levels across future horizons, thereby providing operators with forward-looking decision support.

Accurate load forecasting forms the cornerstone of any reliable risk assessment framework, as it provides essential predictive inputs for modeling future operational conditions. Conventional forecasting techniques—such as regression models (Momani et al., 2024) and autoregressive integrated moving average (ARIMA) models (Abreu et al., 2016)—often struggle to handle the nonlinear and high-dimensional characteristics of modern load data. In recent years, artificial intelligence (AI) methods, notably long short-term memory (LSTM) networks (Murali et al., 2024) and convolutional neural networks (CNN) (Wan et al., 2023), have achieved remarkable success in nonlinear sequence modeling, driving the paradigm shift from deterministic point forecasting to probabilistic forecasting (Xu and Chen, 2024). Probabilistic forecasting explicitly characterizes the uncertainty distribution of future loads, thereby providing richer information for operational risk evaluation. This has spurred the development of various approaches, including DeepAR (Salinas et al., 2020), Q-mixer (Ryu and Yu, 2024), and other advanced frameworks tackling different aspects of uncertainty (Dang et al., 2022). However, existing approaches still face challenges in improving

probabilistic accuracy and effectively capturing complex stochastic dependencies. To overcome these limitations, this paper proposes an enhanced DeepAR-based ultra-short-term probabilistic forecasting model. The conventional linear mapping layers are replaced by the Kolmogorov–Arnold Network (KAN), which places learnable activation functions on edges rather than nodes. This design enhances parameter efficiency and nonlinear approximation capability, thereby granting the model a superior ability to capture complex dependencies. As a result, it provides more accurate and informative forecasts for subsequent dynamic risk assessment.

Following accurate risk quantification, the optimal distribution of flexible resources for proactive control becomes the next critical challenge to ensure system security (Zhu et al., 2025), (Cao et al., 2025). Energy storage systems (ESS), owing to their fast and bidirectional active/reactive power regulation capabilities, play a pivotal role in voltage support (Deng et al., 2024), power flow optimization (Gangil et al., 2024), and fault recovery (Li et al., 2024) within distribution systems. For instance (Gangil et al., 2024), focuses on minimizing total operational cost and power losses for the optimal scheduling of battery energy storage systems (BESS). Separately (Li et al., 2024), targets maximizing a satisfaction-based performance index for fault recovery. Nevertheless, most existing works adopt simplified single-phase network models or focus primarily on economic optimization, often neglecting power quality concerns such as three-phase unbalance and the integration of explicit risk indicators into the control objective. To address these gaps, this paper develops a three-phase energy storage optimization model that minimizes comprehensive operational risk by jointly considering voltage deviations, unbalances, and overload conditions. The model enables risk-aware and proactive control, thereby achieving refined regulation of the low-voltage distribution network's operational state.

To address the operational security and power quality challenges in low-voltage distribution networks, this paper proposes an integrated analytical and decision-making framework, as shown in Figure 1. This integrated approach offers a quantifiable basis for proactive risk management and control decisions in practical grid operations. The main contributions of this paper are as follows:

1. The DeepAR forecasting model is improved by introducing a KAN module to enhance load forecasting accuracy and the ability to capture complex probabilistic features;
2. A dynamic assessment framework integrating voltage deviation, three-phase unbalance, and overloading risks is constructed, achieving comprehensive quantification of multiple risk indicators;
3. A three-phase energy storage optimization model with the goal of minimizing comprehensive risk is established, enhancing the low-voltage distribution network's proactive response capability through risk-optimization control.

The remaining sections of this paper are organized as follows: Section 2 introduces the improved DeepAR ultra-short-term load forecasting model; Section 3 introduces the comprehensive risk assessment framework; Section 4 describes the construction of the three-phase energy storage optimization model; Section 5 verifies the effectiveness of the proposed framework through case studies; Section 6 summarizes the full paper.

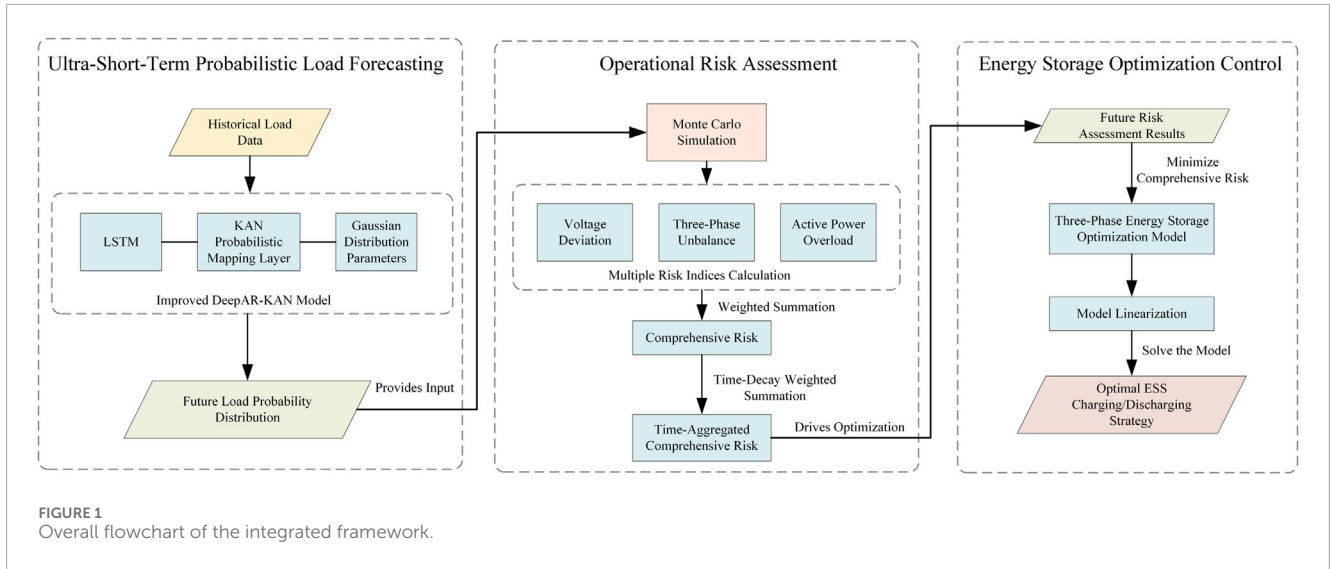


FIGURE 1 Overall flowchart of the integrated framework.

2 Ultra-short-term load forecasting

Ultra-short-term load forecasting is an important foundation for operational risk assessment and optimal control in low-voltage distribution networks. As the uncertainty and complexity of distribution network operational states increase significantly, higher requirements are placed on load forecasting accuracy. To improve the accuracy of ultra-short-term load forecasting, this paper introduces structural improvements to the original DeepAR model. The fully connected layers following the LSTM module in the original DeepAR are replaced with a KAN module to enhance its nonlinear mapping capability and improve the model's forecasting accuracy.

2.1 Long short-term memory network

LSTM is a special type of recurrent neural network (RNN). By introducing gating mechanisms, it significantly mitigates the gradient vanishing or explosion problems common in traditional RNNs during long-sequence modeling. The key to LSTM lies in its cell structure, which mainly includes a forget gate, an input gate, and an output gate. These gating mechanisms effectively filter, memorize, and regulate the output of historical information. Specifically, the processes for each gate and state update are as follows:

1. Forget Gate: controls the proportion of the previous cell state to be retained, as shown in Equation 1.

$$f_t = \sigma(W_f \cdot [h_{t-1}, x_t] + b_f) \tag{1}$$

2. Input Gate: regulates the degree to which current input information updates the cell state, as shown in Equations 2, 3.

$$i_t = \sigma(W_i \cdot [h_{t-1}, x_t] + b_i) \tag{2}$$

$$\tilde{c}_t = \tanh(W_c \cdot [h_{t-1}, x_t] + b_c) \tag{3}$$

3. Cell State Update: updates the cell state by combining the results of the forget gate and input gate, as shown in Equation 4.

$$c_t = f_t * c_{t-1} + i_t * \tilde{c}_t \tag{4}$$

4. Output Gate: controls the influence of the current cell state on the final output, as shown in Equations 5, 6.

$$o_t = \sigma(W_o \cdot [h_{t-1}, x_t] + b_o) \tag{5}$$

$$h_t = o_t * \tanh(c_t) \tag{6}$$

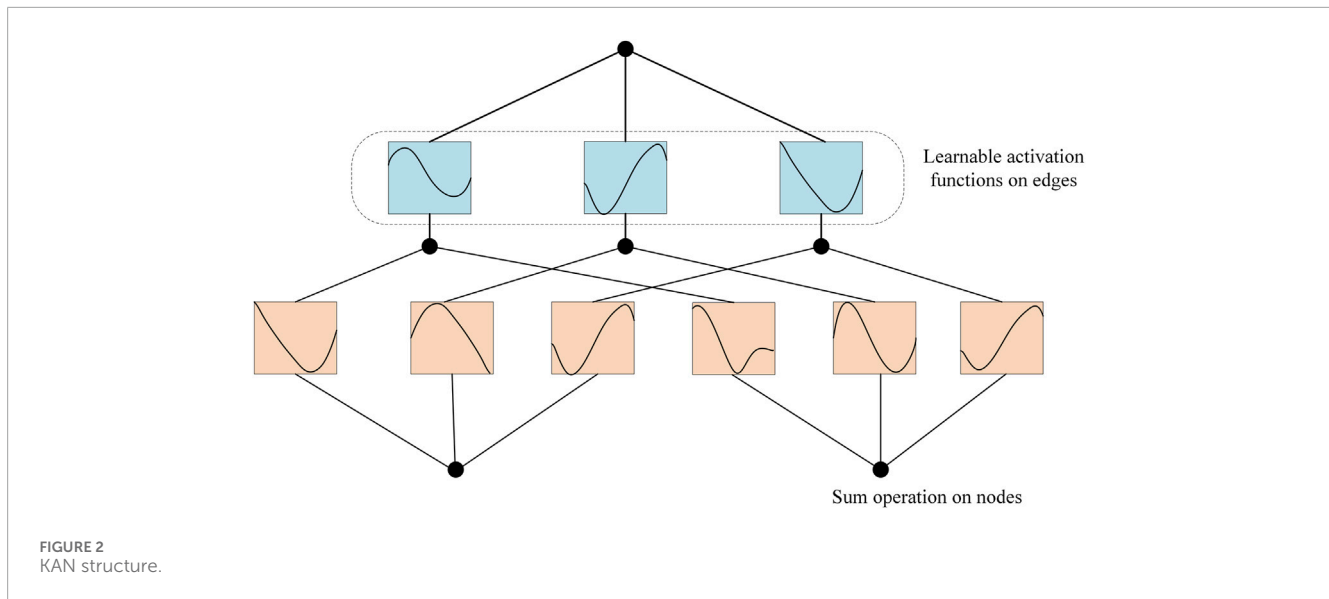
Where W_f , W_i , W_c , W_o are the weight matrices for the forget gate, input gate, cell state, and output gate, respectively; b_f , b_i , b_c , b_o are the bias vectors for the forget gate, input gate, cell state, and output gate, respectively.

2.2 Kolmogorov-Arnold network

The KAN is a novel neural network architecture derived from the Kolmogorov-Arnold representation theorem (Liu Z. et al., 2025), as shown in Equation 7.

$$f(x) = f(x_1, \dots, x_n) = \sum_{q=1}^{2n+1} \Phi_q \left(\sum_{p=1}^n \phi_{q,p}(x_p) \right) \tag{7}$$

Where (x_1, \dots, x_n) is the input vector; n is the dimension of the input vector; Φ_q is a one-dimensional continuous function; and $\phi_{q,p}$ is a one-dimensional continuous function on the interval $[0, 1]$.



Unlike traditional multi-layer perceptron (MLP) that apply fixed activation functions to nodes, KAN places learnable activation functions on the edges of the network, while nodes perform simple summation operations. This design allows it to approximate complex functions with higher parameter efficiency and better accuracy. Its network structure is shown in Figure 2.

In the actual computation of the network, the value of the j -th neuron in the l -th layer, denoted as $x_j^{(l)}$, is obtained by summing the outputs of all neurons in the previous layer $x_i^{(l-1)}$, after being processed by learnable univariate functions, as shown in Equation 8.

$$x_j^{(l)} = \sum_{i=1}^{n_{l-1}} \phi_{j,i}^{(l)}(x_i^{(l-1)}) \quad (8)$$

Where n_{l-1} is the number of neurons in the previous layer, and $\phi_{j,i}^{(l)}$ represents the learnable univariate function defined on the edge connecting the i -th neuron of the previous layer to the j -th neuron of the l -th layer.

2.3 DeepAR probabilistic forecasting model and its improvement

DeepAR is a probabilistic forecasting method based on an autoregressive recurrent network proposed by Salinas (Salinas et al., 2020). It learns shared temporal features by jointly training on a large number of related time series and directly generates the conditional probability distribution of future observations, thereby quantifying uncertainty. The core of the DeepAR model lies in learning the conditional probability distribution of the sequence and decomposing this joint distribution into a product of likelihood factors, as shown in Equation 9.

$$P(z_{i,t_0:T} | z_{i,1:t_0-1}, x_{i,1:T}) = \prod_{t=t_0}^T P(z_{i,t} | \theta(h_{i,t})) \quad (9)$$

Where $z_{i,t}$ is the value of the i -th time series at time t ; t_0 is the forecast start time; $x_{i,1:T}$ are known covariates; $\theta(h_{i,t})$ are the

distribution parameters mapped from the recurrent neural network's hidden state $h_{i,t}$.

In the original DeepAR model, the mapping function for the distribution parameters is typically implemented by fully connected layers. Given that the load is a continuous variable, its forecast uncertainty is parameterized by a Gaussian distribution in this paper (Huang et al., 2023) (Liu M. et al., 2025). The calculations for the distribution's mean and standard deviation are shown in Equations 10, 11.

$$\mu(h_{i,t}) = w_\mu^\top h_{i,t} + b_\mu \quad (10)$$

$$\sigma(h_{i,t}) = \log(1 + \exp(w_\sigma^\top h_{i,t} + b_\sigma)) \quad (11)$$

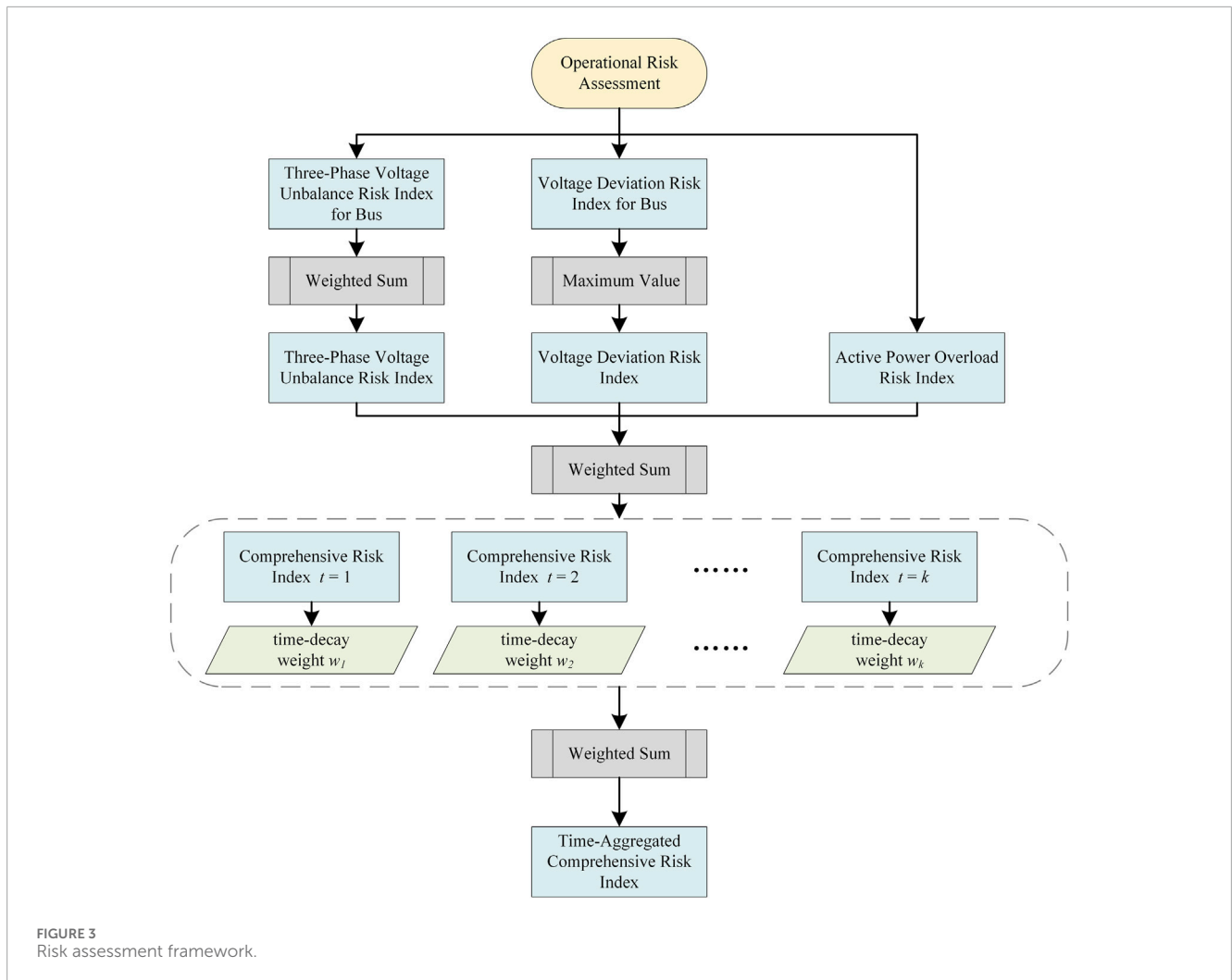
Where μ, σ are the mean and standard deviation of the Gaussian distribution, respectively; w_μ, w_σ are the weight vectors for the mean and standard deviation, respectively; b_μ, b_σ are the bias terms for the mean and standard deviation, respectively.

The conventional fully connected layers in the DeepAR model employ fixed activation functions on nodes. This structure can be limited in flexibility and parameter efficiency when mapping the hidden state to the parameters of complex probability distributions. To overcome this limitation and enhance the model's ability to capture the intricate stochastic characteristics of load data, this paper uses KAN to replace the fully connected mapping layers in the original model. The improved parameter calculation formulas are shown in Equations 12, 13.

$$\mu(h_{i,t}) = \text{KAN}_\mu(h_{i,t}) \quad (12)$$

$$\sigma(h_{i,t}) = \log(1 + \exp(\text{KAN}_\sigma(h_{i,t}))) \quad (13)$$

Where KAN_μ and KAN_σ are independent KAN networks. By using learnable activation functions on edges, KAN achieves a more flexible and efficient nonlinear feature transformation of the input hidden state. This structure enables the model to better capture the complex probabilistic characteristics of



load data, thereby improving the reliability of probabilistic forecasts and providing a more accurate quantification of forecast uncertainty.

3 Risk assessment

To assess the operational risk of low-voltage distribution networks over future periods, this paper proposes a comprehensive risk assessment framework, as shown in Figure 3. This framework focuses on three significant risk types: voltage deviation, three-phase unbalance, and active power overloading. First, the voltage deviation and three-phase unbalance risks at each bus are assessed independently to obtain corresponding bus-level risk indicators. Second, the maximum value method and the weighted summation method are used to synthesize bus-level indicators into system-level indicators. Simultaneously, the active power overloading risk of the transformer is assessed. Then, these three risk indicators are combined via weighted summation to obtain the comprehensive indicator for each future time point. Finally, time-decay weights are used to aggregate the comprehensive indicators across all time points within the period, generating the time-aggregated indicator for that period.

3.1 Risk assessment index

Assessing the risk of a power system under a specific operational state requires considering both the probability of risk occurrence and the severity of its consequences, to construct a quantitative risk indicator that integrates probability and severity (Ji et al., 2020). This paper uses a risk-seeking utility function to quantify risk severity (Yu et al., 2024), and defines the risk indicator as the product of severity and occurrence probability.

1. Three-Phase Voltage Unbalance Risk Index (TVURI): the unbalanced state of three-phase voltages is often assessed using the phase voltage unbalance factor. Referring to IEEE std 936–1987, this paper calculates the three-phase voltage unbalance factor as the ratio of the range of phase voltages (U_A , U_B , U_C) to their average value, as shown in Equations 14, 15.

$$U_{avg} = \frac{U_A + U_B + U_C}{3} \quad (14)$$

$$\varepsilon = \frac{\max(U_A, U_B, U_C) - \min(U_A, U_B, U_C)}{U_{avg}} \quad (15)$$

Where U_A, U_B, U_C are the phase voltages of phases A, B, and C, respectively; U_{avg} is the average three-phase voltage; ε is the three-phase voltage unbalance factor.

The risk-seeking utility function shown in Equation 16 is used to calculate the severity of the three-phase unbalance risk for each operational scenario.

$$S_{unb,i,s} = \frac{e^{\varepsilon_{i,s}} - 1}{e^{\varepsilon_{lim}} - 1} \quad (16)$$

This exponential function is characterized by a progressively increasing slope, which embodies a risk-seeking attitude. As the unbalance factor $\varepsilon_{i,s}$ grows, the severity increases at an accelerating rate. This convex property assigns disproportionately higher scores to severe unbalance conditions. It thus directs control actions to prioritize the most severe cases. This approach is well-established in power system risk assessment to enhance security, as it aligns with the operational priority of preventing significant power quality deterioration (Hu et al., 2023).

The product of this severity and the scenario probability is the TVURI for bus (TVURI(B)), as shown in Equation 17. The TVURI is obtained by weighting and summing the TVURI(B) of all buses, as shown in Equation 18.

$$R_{TVURI(B),i} = \sum_s p_s \cdot S_{unb,i,s} \quad (17)$$

$$R_{TVURI} = \frac{\sum_{i=1}^N w_i \cdot R_{TVURI,i}}{\sum_{i=1}^N w_i} \quad (18)$$

Where $\varepsilon_{i,s}$ is the unbalance factor at bus i under scenario s ; ε_{lim} is the unbalance factor threshold; $S_{unb,i,s}$ is the severity of three-phase unbalance at bus i under scenario s ; p_s is the occurrence probability of scenario s ; $R_{TVURI(B),i}$ is the TVURI(B) value for bus i ; w_i is the weight of bus i ; N is the total number of buses; R_{TVURI} is the TVURI value.

2. Voltage Deviation Risk Index (VDRI): voltage deviation refers to the deviation of the bus voltage from its rated value. Low-voltage distribution networks often have a radial structure, where voltage levels typically decrease along the feeder from the source to the end, making the feeder end more prone to voltage deviation risk. Based on this characteristic, this paper uses the maximum value method for voltage deviation risk assessment in low-voltage distribution networks to highlight the maximum risk point and provide key warnings for operators. First, calculate the voltage deviation risk severity for each phase voltage at each bus.

The calculation of the VDRI follows a three-step procedure. First, the risk severity for each phase voltage at every bus is computed. Then, the severity for the entire bus is defined as the maximum value among its three phases, as given in Equations 19–22. Subsequently, the VDRI for bus (VDRI(B)) is calculated by Equation 23. Finally, the system-wide VDRI is determined as the maximum value across all VDRI(B) values, according to Equation 24.

$$S_{A,i,s} = \frac{e^{|u_{A,i,s} - u_{A,N}|} - 1}{e^{u_{lim}} - 1} \quad (19)$$

$$S_{B,i,s} = \frac{e^{|u_{B,i,s} - u_{B,N}|} - 1}{e^{u_{lim}} - 1} \quad (20)$$

$$S_{C,i,s} = \frac{e^{|u_{C,i,s} - u_{C,N}|} - 1}{e^{u_{lim}} - 1} \quad (21)$$

$$S_{u,i,s} = \max(S_{A,i,s}, S_{B,i,s}, S_{C,i,s}) \quad (22)$$

$$R_{VDRI(B),i} = \sum_s p_s \cdot S_{u,i,s} \quad (23)$$

$$R_{VDRI} = \max_i R_{VDRI(B),i} \quad (24)$$

Where $u_{A,i,s}, u_{B,i,s}, u_{C,i,s}$ are the per-unit voltages of phase A, B and C at bus i under scenario s , respectively; $u_{A,N}, u_{B,N}, u_{C,N}$ are the rated voltages of phases A, B, C, respectively; u_{lim} is the voltage deviation threshold; $S_{A,i,s}, S_{B,i,s}, S_{C,i,s}$ are the voltage deviation risk severities for phases A, B, C at bus i under scenario s , respectively; $S_{u,i,s}$ is the voltage deviation risk severity for bus i under scenario s ; $R_{VDRI(B),i}$ is the VDRI(B) value for bus i ; R_{VDRI} is the VDRI value.

3. Active Power Overload Risk Index (APORI): active power overload risk refers to the situation where the load of a transformer or line exceeds its rated capacity, potentially leading to equipment overheating or accelerated aging. This paper defines the APORI for the transformer, as shown in Equations 25, 26.

$$S_{P,s} = \frac{e^{\max(\rho_s - 1, 0)} - 1}{e^{\rho_{lim}} - 1} \quad (25)$$

$$R_{APORI} = \sum_s p_s \cdot S_{P,s} \quad (26)$$

Where ρ_s is the transformer load rate under scenario s , considering three-phase total load; ρ_{lim} is the overload threshold; $S_{P,s}$ is the active power overload severity under scenario s ; R_{APORI} is the APORI value.

To operationalize this risk quantification, the proposed framework leverages the probabilistic load forecasts from Section 2. A large set of equiprobable future load scenarios is first generated by Monte Carlo simulation, sampling from the forecasted probability distributions. Subsequently, the value of each risk index is computed as the expected value of its corresponding severity across all simulated scenarios, thereby propagating the load forecast uncertainty directly into the final risk estimates.

3.2 Comprehensive risk index

A weighted sum of the above three risk indicators yields the comprehensive risk index (CRI) for each time point, as shown in Equation 27.

$$R_{CRI} = w_{unb} \cdot R_{TVURI} + w_u \cdot R_{VDRI} + w_p \cdot R_{APORI} \quad (27)$$

Where w_{unb}, w_u, w_p are the weights for the TVURI, VDRI, and APORI indicators, respectively; R_{CRI} is the CRI value.

The determination of these weights can be guided by various methods, such as analytical hierarchy process (AHP) or expert elicitation, reflecting the relative importance of different risk types based on specific operational priorities. In this study, the weights are assigned based on engineering judgment to balance the concerns

of power quality and equipment security for the considered case study.

Nonlinear aggregation methods or risk-averse formulations are viable alternatives. However, the linear weighted sum is adopted here for its interpretability and computational simplicity. This approach aligns with the practical need for a straightforward and transparent risk indicator in operational contexts. Future work could explore the comparative performance of different aggregation schemes.

3.3 Time-aggregated comprehensive risk index

The weighted summation method is used to aggregate the CRI over a given period, resulting in the time-aggregated composite risk index (TACRI), as shown in Equation 28. An exponential time-decay weight is used to aggregate the risk indicators over a future period, as shown in Equation 29. This approach accounts for the greater influence of near-term risks on current decisions compared to distant ones.

$$R_{TACRI} = \frac{\sum_t w_t \cdot R_{CRI,t}}{\sum_t w_t} \quad (28)$$

$$w_t = e^{-\lambda(t-1)} \quad (29)$$

Where t is the time step index; w_t is the weight for the t -th time step; λ is the time decay coefficient; $R_{CRI,t}$ is the CRI value at the t -th time step; R_{TACRI} is the TACRI value.

The coefficient λ determines the temporal preference of the risk assessment. A larger λ value results in a steeper exponential decay, causing the aggregation to focus more heavily on immediate short-term risks. This is suitable for operational decisions requiring rapid response, such as real-time control. Conversely, a smaller λ value leads to a more gradual decay, distributing weight more evenly across future time steps. This is appropriate for planning purposes where a longer-term perspective is needed. In practice, the value of λ is typically chosen based on the decision-making horizon and the desired balance between reacting to immediate threats and considering future trends.

Under normal operating conditions where all physical limits (ϵ_{lim} , u_{lim} , ρ_{lim}) are satisfied, the risk severity functions yield values between 0 and 1, consequently bounding the CRI between 0 and 1. However, if any of these limits are exceeded, the employed risk-seeking utility functions can produce severity values greater than 1, leading to a CRI that may also exceed 1. This design intentionally amplifies the risk score for out-of-limit conditions to alert operators. The TACRI, as a time-weighted average of CRI values across a period, inherits this numerical characteristic.

It is worth mentioning that the proposed risk assessment framework is not limited to the assessment of the three distribution network operational risks above. The framework has strong extensibility and can provide a unified assessment approach for other distribution network operational risks. Furthermore, the core aggregation methodology can also be adapted to incorporate nonlinear or other advanced fusion techniques in future applications. In practical applications, suitable severity quantification functions and probability models can be designed

according to the specific characteristics of particular risks. The processes of multi-indicator synthesis and time aggregation can be reused to achieve a holistic or hierarchical assessment of multiple risks. This demonstrates the applicability and flexibility of the proposed assessment method in different scenarios.

4 Energy storage optimization

To mitigate voltage deviation, three-phase unbalance, and transformer overload in low-voltage distribution networks, this paper constructs an optimal operation model with ESS as the core regulating resource. This model adopts a three-phase decoupled modeling approach, which can more accurately describe the operational state of asymmetric distribution networks, and achieves refined control of system operational risk through coordinated control of ESS charging and discharging power.

4.1 Objective function

The proposed low-voltage distribution network optimal operation model aims to minimize the comprehensive operational risk. To reduce the complexity of the optimization model, simplified equivalent calculations are applied to the three risk indicators. The model's objective function is shown in Equation 30.

$$\begin{aligned} \min & w_u \cdot \sum_{t \in T} \sum_{i \in N} \sum_{p \in \phi} \left| \frac{(U_{i,t}^p)^2 - (U_N)^2}{2U_N} \right| \\ & + w_{unb} \cdot \sum_{t \in T} \sum_{i \in N} \sum_{p_1 \neq p_2} \left| \frac{(U_{i,t}^{p_1})^2 - (U_{i,t}^{p_2})^2}{2U_N^2} \right| \\ & + w_p \cdot \sum_{t \in T} \sum_{g \in G_{tran}} \left(\frac{\sum_{p \in \phi} P_{g,t}^p}{P_{tran(g),rate}} - 1 \right) \end{aligned} \quad (30)$$

Where t is the time index; T is the optimization dispatch period; i is the bus index; N is the set of system buses; p is the phase index; g is the generator index; G_{tran} is the set of equivalent generator; $U_{i,t}^p$ is the voltage at phase p of bus i in period t ; U_N is the rated voltage; $P_{g,t}^p$ is the active power output at phase p of generator g in period t ; $P_{tran(g),rate}$ is the rated power of the distribution transformer within equivalent generator g .

The objective function's three terms penalize voltage deviation from the rated value, three-phase voltage unbalance, and transformer active power overload, respectively. These penalized physical quantities are the direct inputs to the risk severity functions defined in Section 3.1. In this simplified model, the transformer connected to the main grid and its high-voltage side power source are unified as an equivalent generator at that bus. The transformer's active load rate is approximately equal to the ratio of the total active power output of this equivalent generator to the transformer's rated capacity.

4.2 Model constraints

1. Branch Power Flow Constraints: this paper uses the DistFlow model based on second-order cone relaxation (SOCP) (Su et al., 2023), as shown in Equations 31, 32.

TABLE 1 Point forecast evaluation results of different models.

Model	MAE	RMSE	MAPE	R ²
BPNN	40.4758	53.4488	3.08%	0.8095
GRU	48.4646	65.8770	3.62%	0.6840
LSTM	38.4855	52.8476	2.89%	0.8120
Original DeepAR	38.4343	51.6059	2.91%	0.8159
Proposed model	37.8289	51.3254	2.85%	0.8217

$$(U_{jt}^p)^2 - (U_{it}^p)^2 + 2(R_{ij}^p P_{ij,t}^p + X_{ij}^p Q_{ij,t}^p) - ((R_{ij}^p)^2 + (X_{ij}^p)^2) \cdot (I_{ij,t}^p)^2 = 0 \quad \forall p, t, (i, j) \quad (31)$$

$$(2P_{ij,t}^p)^2 + (2Q_{ij,t}^p)^2 + (I_{ij,t}^p - U_{it}^p)^2 \leq (I_{ij,t}^p + U_{it}^p)^2 \quad \forall p, t, (i, j) \quad (32)$$

Where i, j are bus indices; (i, j) denotes the branch connecting bus i and bus j ; R_{ij}^p, X_{ij}^p are the resistance and reactance of branch (i, j) on phase p , respectively; $I_{ij,t}^p, P_{ij,t}^p, Q_{ij,t}^p$ are the current, active power flow, and reactive power flow of branch (i, j) on phase p in period t , respectively.

2. Power Balance Constraints: the system must maintain active and reactive power balance at all times, as shown in Equations 33, 34.

$$\sum_{g \in G_i} P_{g,t}^p + \sum_{ess \in ESS_i} (P_{ess,t}^{dis,p} - P_{ess,t}^{ch,p}) - P_{load,i,t}^p = \sum_{(i,j) \in L} P_{ij,t}^p - \sum_{(k,i) \in L} (P_{ki,t}^p - R_{ki}^p (I_{ki,t}^p)^2) \quad \forall p, t, i \quad (33)$$

$$\sum_{g \in G_i} Q_{g,t}^p + \sum_{ess \in ESS_i} Q_{ess,t}^p - Q_{load,i,t}^p = \sum_{(i,j) \in L} Q_{ij,t}^p - \sum_{(k,i) \in L} (Q_{ki,t}^p - X_{ki}^p (I_{ki,t}^p)^2) \quad \forall p, t, i \quad (34)$$

Where i, j, k are bus indices; L is the set of branches; G_i is the set of generators connected to bus i ; $P_{g,t}^p, Q_{g,t}^p$ are the active and reactive power outputs of generator g on phase p in period t , respectively; ess is the ESS index; ESS_i is the set of ESS connected to bus i ; $P_{ess,t}^{dis,p}, P_{ess,t}^{ch,p}$ are the discharging and charging active power of ESS ess on phase p in period t , respectively; $Q_{ess,t}^p$ is the reactive power output of ESS ess on phase p in period t ; $P_{load,i,t}^p, Q_{load,i,t}^p$ are the active and reactive loads at phase p of bus i in period t , respectively.

3. ESS Constraints: ESS constraints include its state of charge (SOC) related constraints, as shown in Equations 35, 36; relaxed charging/discharging power limits and reactive power limits, as shown in Equations 37–42; exclusive charging/discharging constraint, as shown in Equation 43; SOC limits at the beginning and end of the optimization period, as shown in Equations 44, 45.

$$SOC_{ess,t} = SOC_{ess,t-1} + \left(\eta_{ess}^{ch} \cdot \sum_{p \in \phi} P_{ess,t}^{ch,p} \cdot \Delta t - \frac{\sum_{p \in \phi} P_{ess,t}^{dis,p}}{\eta_{ess}^{dis}} \cdot \Delta t \right) / E_{ess} \quad \forall ess, t > 1 \quad (35)$$

$$SOC_{ess}^{\min} \leq SOC_{ess,t} \leq SOC_{ess}^{\max} \quad \forall ess, t \quad (36)$$

$$0 \leq P_{ess,t}^{dis,p} \leq u_{ess,t}^{dis} \cdot \frac{\sqrt{2}}{2} S_{ess}^{\max} \quad \forall ess, p, t \quad (37)$$

$$0 \leq P_{ess,t}^{ch,p} \leq u_{ess,t}^{ch} \cdot \frac{\sqrt{2}}{2} S_{ess}^{\max} \quad \forall ess, p, t \quad (38)$$

$$0 \leq \sum_{p \in \phi} P_{ess,t}^{dis,p} \leq u_{ess,t}^{dis} \cdot \frac{\sqrt{2}}{2} S_{ess}^{\max} \quad \forall ess, t \quad (39)$$

$$0 \leq \sum_{p \in \phi} P_{ess,t}^{ch,p} \leq u_{ess,t}^{ch} \cdot \frac{\sqrt{2}}{2} S_{ess}^{\max} \quad \forall ess, t \quad (40)$$

$$-\frac{\sqrt{2}}{2} S_{ess}^{\max} \leq Q_{ess,t}^p \leq \frac{\sqrt{2}}{2} S_{ess}^{\max} \quad \forall ess, p, t \quad (41)$$

$$-\frac{\sqrt{2}}{2} S_{ess}^{\max} \leq \sum_{p \in \phi} Q_{ess,t}^p \leq \frac{\sqrt{2}}{2} S_{ess}^{\max} \quad \forall ess, t \quad (42)$$

$$u_{ess,t}^{dis} + u_{ess,t}^{ch} \leq 1 \quad \forall ess, t \quad (43)$$

$$SOC_{ess,1} = SOC_{ess,0} + \left(\eta_{ess}^{ch} \cdot \sum_{p \in \phi} P_{ess,t}^{ch,p} \cdot \Delta t - \frac{\sum_{p \in \phi} P_{ess,t}^{dis,p}}{\eta_{ess}^{dis}} \cdot \Delta t \right) / E_{ess} \quad \forall ess \quad (44)$$

$$SOC_{ess,|T|} \geq \alpha \cdot SOC_{ess,0} \quad \forall ess \quad (45)$$

Where $SOC_{ess,t}$ is the SOC of ESS ess in period t ; $SOC_{ess,0}$ is the initial SOC of ESS ess before optimization; $SOC_{ess}^{\min}, SOC_{ess}^{\max}$ are the lower and upper limits of ESS ess , respectively; $\eta_{ess}^{ch}, \eta_{ess}^{dis}$ are the charging and discharging efficiencies of ESS ess , respectively; E_{ess} is the rated capacity of ESS ess ; Δt is the time interval; $u_{ess,t}^{ch}, u_{ess,t}^{dis}$ are the 0–1 state variables for charging and discharging of ESS ess , respectively; S_{ess}^{\max} is the maximum apparent power of the ESS; α is a parameter related to SOC change of ESS.

4. Generator Constraints: include the upper and lower limits for the active and reactive power outputs of generator units, as shown in Equations 46–49.

$$P_g^{\min} \leq P_{g,t}^p \leq P_g^{\max} \quad \forall g, p, t \quad (46)$$

$$P_g^{\min} \leq \sum_{p \in \phi} P_{g,t}^p \leq P_g^{\max} \quad \forall g, t \quad (47)$$

$$Q_g^{\min} \leq Q_{g,t}^p \leq Q_g^{\max} \quad \forall g, p, t \quad (48)$$

$$Q_g^{\min} \leq \sum_{p \in \phi} Q_{g,t}^p \leq Q_g^{\max} \quad \forall g, t \quad (49)$$

Where P_g^{\min}, P_g^{\max} are the lower and upper limits of active power output for generator g , respectively; Q_g^{\min}, Q_g^{\max} are the lower and upper limits of reactive power output for generator g , respectively.

5. Voltage Constraints: constraints on the magnitude of the voltage at each phase of each bus, as shown in Equation 50.

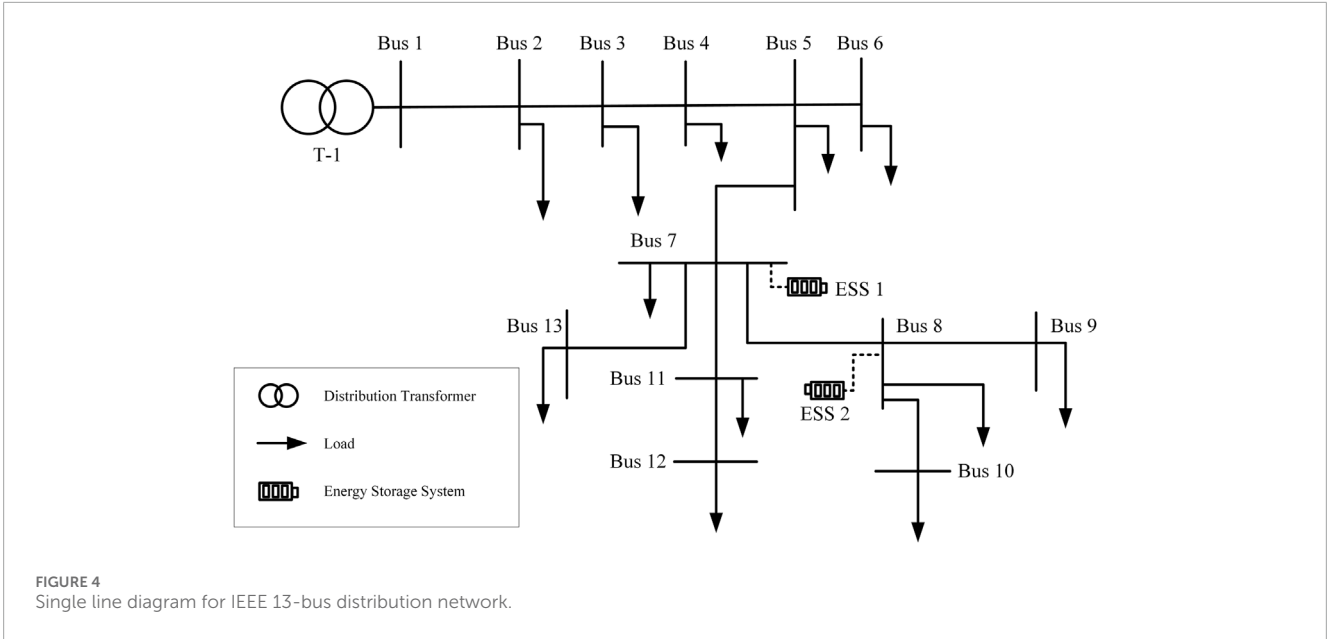


FIGURE 4 Single line diagram for IEEE 13-bus distribution network.

TABLE 2 Risk indicator calculation parameters.

Parameter	ε_{lim}	W_i	U_N	U_{lim}	ρ_{lim}	W_{unb}	W_u	W_p	λ
Value	0.02	1	1.0 p.u.	0.05	0.2	0.4	0.3	0.3	2

$$(U_{min})^2 \leq (U_{i,t}^p)^2 \leq (U_{max})^2 \quad \forall i, t, p \quad (50)$$

Where U_{min} , U_{max} are the lower and upper limits of the voltage magnitude, respectively.

6. Voltage Unbalance Constraint: constraints on the three-phase voltage unbalance degree, as shown in Equation 51.

$$\left| \frac{(U_{i,t}^{p_1})^2 - (U_{i,t}^{p_2})^2}{2U_N^2} \right| \leq \varepsilon_{max} \quad \forall i, t, p_1 \neq p_2 \quad (51)$$

Where ε_{max} is the upper limit for the three-phase unbalance degree.

$$\frac{(U_{i,t}^p)^2 - (U_N)^2}{2U_N} \leq y_{u,i,t}^p \quad \forall i, t, p \quad (53)$$

$$\frac{(U_{i,t}^p)^2 - (U_N)^2}{2U_N} \leq y_{u,i,t}^p \quad \forall i, t, p \quad (54)$$

$$\frac{(U_{i,t}^{p_1})^2 - (U_{i,t}^{p_2})^2}{2U_N^2} \leq y_{unb,i,t}^{p_1,p_2} \quad \forall i, t, p_1 \neq p_2 \quad (55)$$

$$\frac{(U_{i,t}^{p_2})^2 - (U_{i,t}^{p_1})^2}{2U_N^2} \leq y_{unb,i,t}^{p_1,p_2} \quad \forall i, t, p_1 \neq p_2 \quad (56)$$

$$\frac{(U_{i,t}^{p_1})^2 - (U_{i,t}^{p_2})^2}{2U_N^2} \leq \varepsilon_{max} \quad \forall i, t, p_1 \neq p_2 \quad (57)$$

$$\frac{(U_{i,t}^{p_2})^2 - (U_{i,t}^{p_1})^2}{2U_N^2} \leq \varepsilon_{max} \quad \forall i, t, p_1 \neq p_2 \quad (58)$$

4.3 Model linearization

Considering that the first and second terms of the objective function involve absolute value calculations, auxiliary variables $y_{u,i,t}^p$ and $y_{unb,i,t}^{p_1,p_2}$ are introduced for linearization. The processed objective function and constraints are shown in Equations 52–56. Equation 51 is linearized, as shown in Equations 57, 58.

$$\begin{aligned} \min \quad & w_u \cdot \sum_{t \in T} \sum_{i \in N} \sum_{p \in \phi} y_{u,i,t}^p + w_{unb} \cdot \sum_{t \in T} \sum_{i \in N} \sum_{p_1 \neq p_2} y_{unb,i,t}^{p_1,p_2} \\ & + w_p \cdot \sum_{t \in T} \sum_{g \in G_{tran}} \left(\frac{\sum_{p \in \phi} P_{g,t}^p}{P_{tran(g),rate}} - 1 \right) \end{aligned} \quad (52)$$

5 Case study

5.1 Ultra-short-term load forecasting

To verify the reliability of the improved DeepAR model, load data from a low-voltage distribution network in Eastern China for the year 2024 is selected for case analysis. The time span of the load data is from 1 February 2024, to 31 October 2024, with a sampling interval of 15 min, totaling 26,304 samples. The model uses the

TABLE 3 Risk assessment results.

Time	TVURI	VDRI	APORI	CRI	TACRI
16:15	0.1989	0.6915	0.5182	0.4425	0.4415
16:30	0.1383	0.6879	0.5783	0.4352	
16:45	0.0930	0.6809	0.6264	0.4294	
17:00	0.1908	0.7107	0.6714	0.4910	
17:15	0.0438	0.6811	0.7128	0.4357	
17:30	0.2524	0.7423	0.7796	0.5575	
17:45	0.0502	0.6884	0.7897	0.4635	
18:00	0.0680	0.7020	0.8346	0.4882	
18:15	0.0940	0.7045	0.8541	0.5052	
18:30	0.1426	0.7130	0.8543	0.5272	
18:45	0.1111	0.7228	0.8743	0.5236	
19:00	0.1553	0.7195	0.8726	0.5398	
19:15	0.0790	0.7105	0.8625	0.5035	
19:30	0.1257	0.7159	0.8295	0.5139	
19:45	0.0593	0.6995	0.8122	0.4773	
20:00	0.0727	0.6978	0.7792	0.4722	

historical data from the previous 8 h (32 time steps) to forecast the electrical load for the next 4 h (16 time steps). The mean value of the model output is used as the point forecast. Mean absolute error (MAE), root mean square error (RMSE), mean absolute percentage error (MAPE), and the coefficient of determination (R^2) are selected as evaluation metrics.

The improved DeepAR model consists of a 2-layer LSTM (128 neurons per layer) followed by a 1-layer KAN. The KAN has a width of 16, featuring 5 grid points, a spline order of 3, and the SiLU basis function. This final structure is selected based on a series of preliminary experiments that aim to balance model capacity with forecasting performance. The entire model is trained using the negative log-likelihood (NLL) loss function. The forecasting results of the proposed model are compared with typical forecasting models (BPNN, GRU, LSTM) and the original DeepAR model. The typical forecasting models are set with 2 hidden layers, 128 neurons per layer, followed by 2 fully connected layers with 64 neurons each, using the Huber loss function. The dropout rate for all layers is set to 0.2. The total dataset is divided into training, validation, and test sets in a 7:1:2 ratio. The model is trained with a batch size of 128 and a learning rate of 0.001. The number of iterations is not limited, with an early stopping strategy employed to ensure generalization ability. The point forecast evaluation results are shown in Table 1.

As shown in Table 1, the improved model proposed in this paper outperforms the typical forecasting models in all four metrics.

Compared to the LSTM model, the MAE, RMSE, and MAPE of the proposed model decrease by 1.71%, 2.88%, and 1.38%, respectively. Compared to the original DeepAR model, the MAE, RMSE, and MAPE decrease by 1.58%, 0.54%, and 2.06%, respectively. This demonstrates the improvement in load forecasting accuracy of the proposed model compared to both typical forecasting models and the original DeepAR model.

5.2 Comprehensive risk assessment

The IEEE 13-bus distribution network system is used for case analysis. This test system was selected because its scale and radial topology are representative of a typical low-voltage distribution feeder or transformer area, which is often supplied by a single transformer and usually contains around 10 buses. To further align with the study's focus, the transformer at bus 6 is removed to simulate a low-voltage distribution network with a single transformer. Its single-line diagram is shown in Figure 4, which sufficiently illustrates the network connectivity. Line parameters refer to (Aref et al., 2012). The three-phase load data from a specific 12-bus low-voltage distribution network in Eastern China is used as the load of buses 2–13 in the above system. Bus 1 has no local load and is connected to a transformer bank with a total rated capacity of 1,600 kVA (rated active power 1,520 kW). The scope of this case study is confined to networks with conventional loads, thereby excluding the influence of distributed energy resources like photovoltaics or electric vehicles. Other indicator calculation parameters are shown in Table 2. The parameter thresholds for risk calculation are selected according to prevalent industry standards and engineering practice. The weights for the risk indicators are assigned based on engineering judgment to balance the priorities among power quality and equipment security, with a slightly greater emphasis on phase unbalance mitigation in this specific network. The time decay coefficient $\lambda = 2$ is chosen to prioritize the impact of short-term risks on immediate control actions.

Risk assessment analysis is conducted for a typical daily load peak period (16:15–20:00) as an example. This period is selected because it typically exhibits higher operational risks due to increased load demand, making it critical for validating the proposed assessment framework. Based on the Gaussian distribution parameters of the load generated by the probabilistic load forecasting model above, 5,000 Monte Carlo simulations are performed to obtain the three-phase load data for each bus at different times under each scenario. This number aligns with common practice in related power system risk assessment studies to achieve sufficient statistical precision. Without ESS integration, the comprehensive risk indicator for this period is calculated according to the risk assessment framework established in Section 3. The assessment results are shown in Table 3.

From Table 3, it can be seen that TVURI and VDRI peak simultaneously at 17:30. This indicates a significant load unbalance where one phase's load is markedly higher than the other two, causing localized power quality deterioration. APORI remains high from 18:00 to 19:45, consistent with this period being the load peak. CRI exceeds 0.5 at multiple time points, such as 17:30 and from 18:15 to 19:30, indicating high operational risk

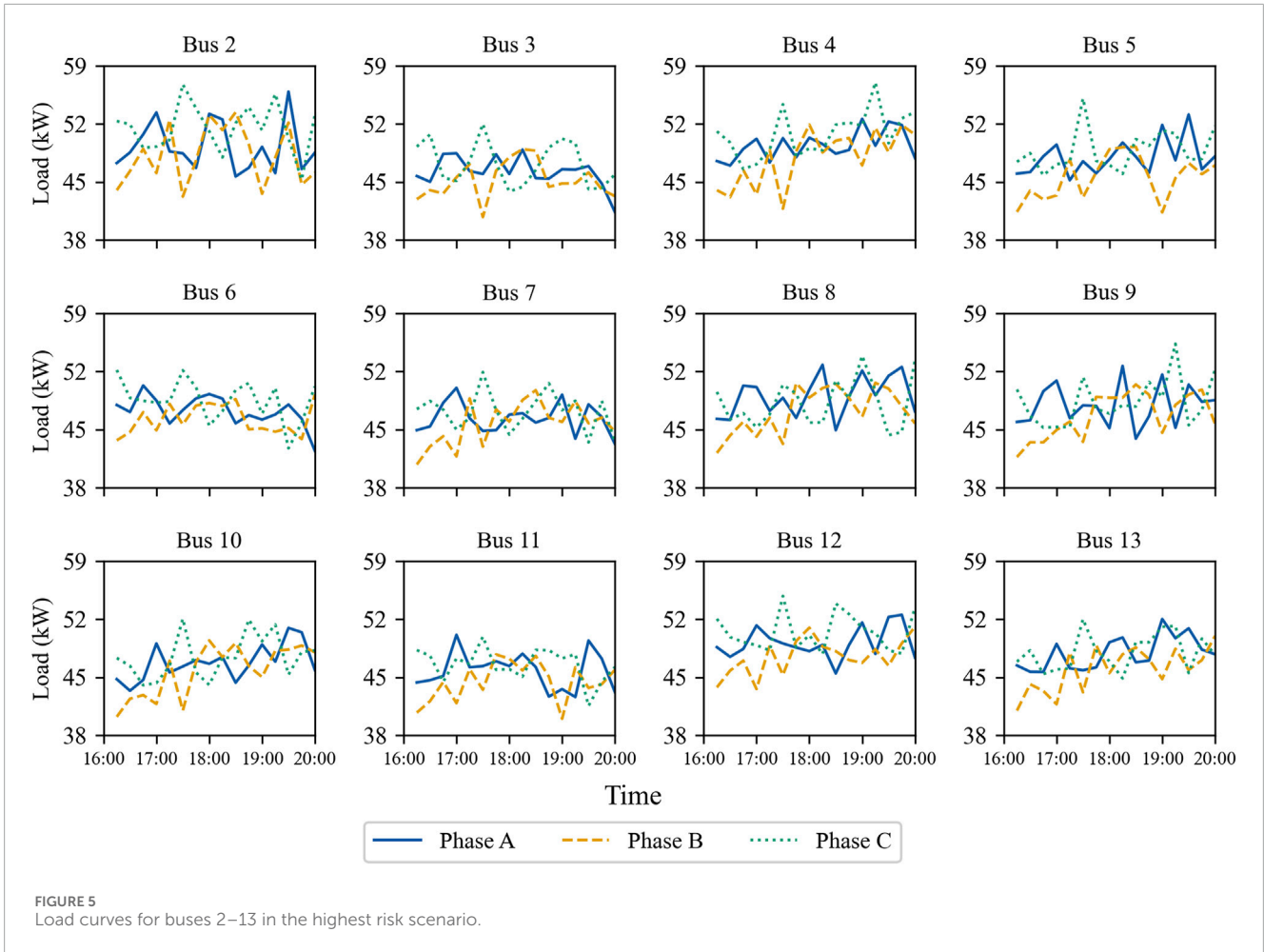
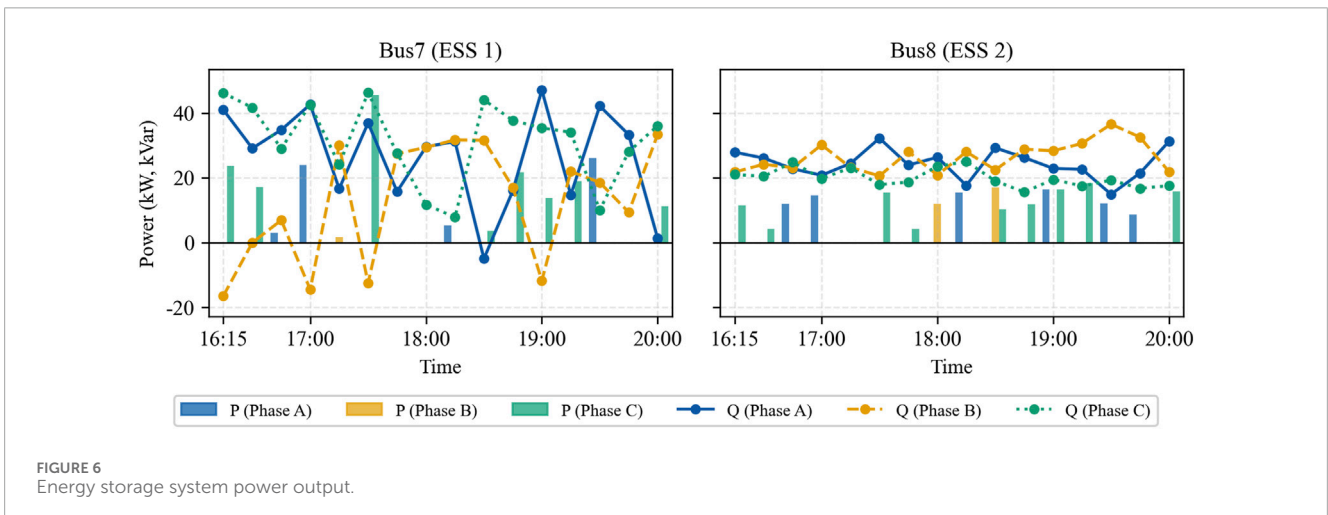
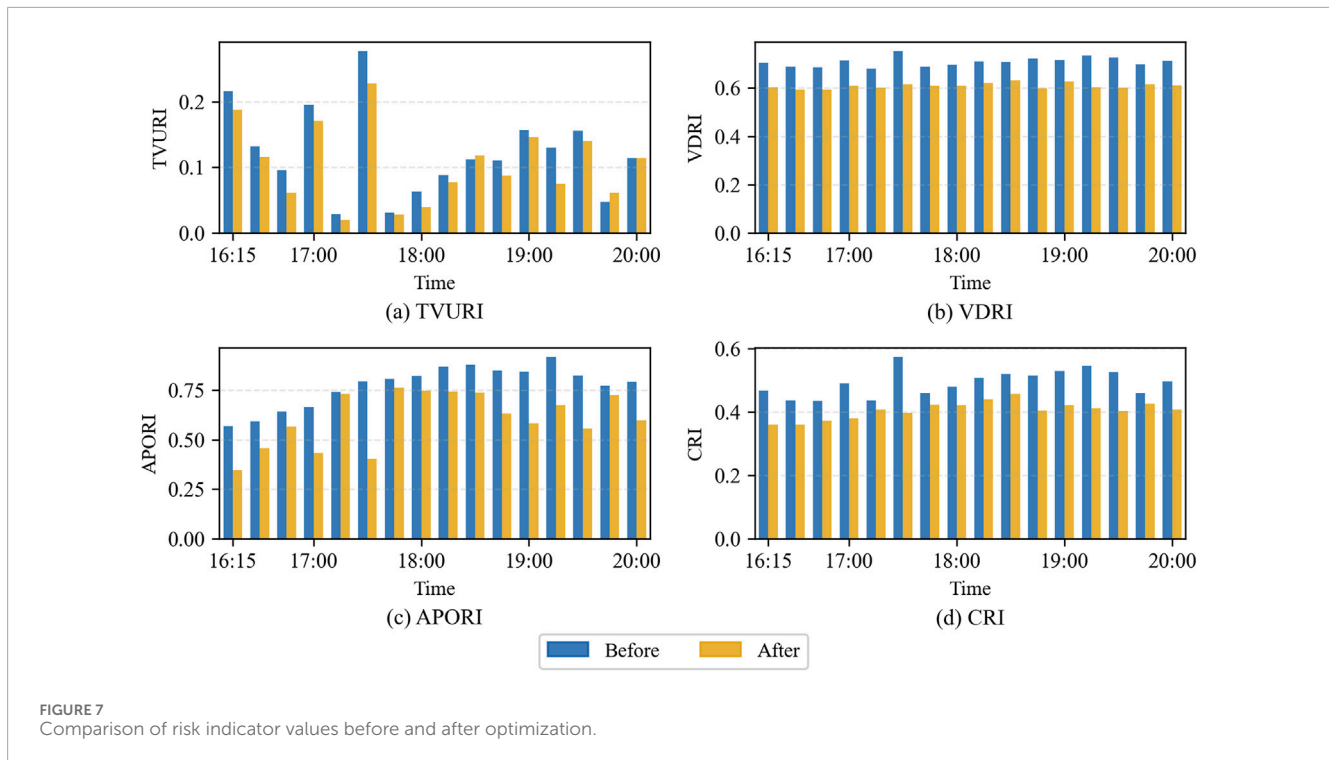


TABLE 4 Parameters of ESS.

Parameter	E_{ess}	SOC_{ess}^{min}	SOC_{ess}^{max}	$SOC_{ess,0}$	S_{ess}^{max}	η_{ess}^{ch}	η_{ess}^{dis}	α
Value	300 kWh	0.1	0.9	0.5	100 kW	0.9	0.9	0.6





at these times. The risk at 17:30 is primarily driven by three-phase unbalance and voltage deviation, while the risk after 18:15 mainly stems from voltage deviation and transformer overload. The TACRI for this load peak period reaches 0.4415, indicating that the system remains at a medium-high risk level throughout the assessment window. This value reflects a certain persistence of risk over time. This analysis shows that the proposed comprehensive risk assessment framework can effectively identify the dominant risk types in different periods, clarify the causes of risks, and provide clear control directions for operators. Through multi-indicator integration and time aggregation, the framework achieves a comprehensive assessment from local to system-wide and from static to dynamic, providing data support for subsequent energy storage optimization control.

5.3 Energy storage optimization

To verify the actual control effect of the proposed energy storage optimization model, the typical high-risk scenario with the highest TACRI value from Section 5.2 is selected as the optimization object. The load time series distribution for buses 2–13 under this scenario is shown in Figure 5. To reflect the coordinated control capability of energy storage, one ESS with identical parameters is configured at each of bus 7 and bus 8. These locations are electrically distant from the source and serve as key feeder branches with significant unbalanced loads, making them effective points for voltage support and unbalance mitigation. The parameters of ESS are shown in Table 4. The capacity of 300 kWh (with 100 kW power rating) is commensurate with the typical phase load range at these buses, providing sufficient energy and power during the peak risk period without over-sizing.

Based on the three-phase energy storage optimization model established in Section 4, this high-risk scenario is optimized and solved. The model is a mixed-integer quadratically constrained program (MIQCP), modeled in GAMS and solved using the Gurobi optimizer. The resulting model comprises 8,405 constraints and 4,081 variables. Using the Gurobi solver, the model is solved to optimality within 5.82 s, demonstrating the computational tractability of the proposed approach for operational timeframes. The resulting active and reactive power output schedules for each ESS over the entire period are shown in Figure 6. Figure 7 compares the values of various risk indicators before and after optimization.

From Figures 6, 7, it can be observed that the optimized output of the ESS significantly reduces system operational risk. After optimization, the average values of TVURI, VDRI, APORI, and CRI decreased by 14.01%, 14.01%, 21.90%, and 17.30%, respectively. Specifically, to address the peaks in TVURI and VDRI at 17:30 caused by a sudden increase in phase C load, the ESS at bus 7 provides effective support by injecting active power into phase C. This support effectively mitigates the localized voltage quality issue and three-phase unbalance phenomenon at that time. Meanwhile, the ESS at bus 8 discharges during the load peak period after 18:00, effectively reducing the transformer's active power overload risk. Applying the ESS output strategy shown in Figure 6 to all simulated scenarios, the calculated TACRI after optimization is 0.3660, a decrease of 17.10% compared to before optimization. This indicates that the optimized ESS output effectively reduces the overall operational risk during this period.

These results demonstrate that the constructed energy storage optimization model can dynamically adjust the active/reactive power output of the ESS based on risk assessment results, achieving precise suppression of future risks. The optimization model provides a feasible security control method for distribution networks with

high penetration of distributed generation. It works by regulating ESS output to address both short-term peak risks and sustained overload risks.

6 Conclusion

Focusing on the operational security and power quality issues of low-voltage distribution networks, this paper proposes an integrated solution. The main work and conclusions are as follows:

1. An improved DeepAR-KAN ultra-short-term probabilistic load forecasting model is proposed. By introducing KAN, the prediction accuracy of the model is improved. Case study shows that this model outperforms comparison models on key metrics such as MAE and RMSE, providing more accurate input for risk assessment.
2. A comprehensive dynamic risk assessment framework is constructed. This framework achieves spatiotemporal aggregation and quantification of voltage deviation, three-phase unbalance, and active power overloading risks. The case study shows that the assessment method successfully quantifies future risks and identifies the dominant risks, verifying the framework's effectiveness and practicality.
3. A three-phase energy storage optimization model aimed at minimizing comprehensive risk is established. The model coordinates ESS for phase-wise compensation. Case results show that the optimized risk indicators are reduced by an average of over 14%, confirming its effectiveness in proactively suppressing operational risks.

In summary, the proposed “forecast-assessment-optimization” framework enhances risk management in low-voltage distribution networks. While validated on a specific case, its modular structure is readily transferable and adaptable to other configurations. This demonstrates its broad application potential. Future work will incorporate uncertainties from distributed PV and electric vehicles, extending the framework to more complex environments.

Data availability statement

The original contributions presented in the study are included in the article/supplementary material, further inquiries can be directed to the corresponding author.

References

- Abreu, T., Ren, C., Lotufo, A. P., and Lopes, M. L. M. (2016). Electrical demand load forecasting by ARIMA regression and artificial neural networks. *Int. J. Comput. Inf. Technol.* 5 (3), 284–289. Available online at: <https://www.ijcit.com/archives/volume5/issue3/Paper050301.pdf>.
- Aref, A., Davoudi, M., Razavi, F., and Davoodi, M. (2012). Optimal DG placement in distribution networks using intelligent systems. *Energy Power Eng.* 4 (2), 92–98. doi:10.4236/epe.2012.42013
- Bie, Z., Bian, Y., Zhang, L., Huang, Y., and Li, G. (2024). Key technologies of risk prevention and emergency management against extreme events for new power systems. *Proc. CSEE* 44 (18), 7049–7068. doi:10.13334/j.0258-8013.pcsee.241046

Author contributions

YL: Writing – original draft, Conceptualization. CL: Writing – original draft, Formal Analysis. SL: Writing – original draft, Investigation. JD: Investigation, Writing – review and editing. YM: Writing – review and editing, Data curation.

Funding

The author(s) declared that this work received funding from State Grid Shanghai Municipal Electric Power Company. This research was funded by science and technology program of State Grid Shanghai Municipal Electric Power Company, grant number 52093324000L and the APC was funded by the same funding. The funder was not involved in the study design, collection, analysis, interpretation of data, the writing of this article, or the decision to submit it for publication.

Conflict of interest

Authors YL, CL, SL, JD, and YM were employed by State Grid Shanghai Municipal Electric Power Company.

Generative AI statement

The author(s) declared that generative AI was not used in the creation of this manuscript.

Any alternative text (alt text) provided alongside figures in this article has been generated by Frontiers with the support of artificial intelligence and reasonable efforts have been made to ensure accuracy, including review by the authors wherever possible. If you identify any issues, please contact us.

Publisher's note

All claims expressed in this article are solely those of the authors and do not necessarily represent those of their affiliated organizations, or those of the publisher, the editors and the reviewers. Any product that may be evaluated in this article, or claim that may be made by its manufacturer, is not guaranteed or endorsed by the publisher.

- Cao, H., Ma, L., Liu, G., Liu, Z., and Dong, H. (2024). Two-stage energy storage allocation considering voltage management and loss reduction requirements in unbalanced distribution networks. *Energies* 17 (24), 6325. doi:10.3390/en17246325

- Cao, K., Liu, Y., and Wang, C. (2025). Coordinated distributionally robust optimal allocation of energy storage system for HV-MV distribution network resilience enhancement. *IEEE Trans. Industry Appl.* 61 (2), 2011–2024. doi:10.1109/tia.2024.3496846

- Chen, Z., Liang, L., and Lu, C. (2025). Optimized coordination of electric vehicles, distributed compensation devices, and distributed generation for risk mitigation in radial distribution networks. *IET Renew. Power Gener.* 19 (1), e70019. doi:10.1049/rpg2.70019

- Dang, S., Peng, L., Zhao, J., Li, J., and Kong, Z. (2022). A quantile regression random forest-based short-term load probabilistic forecasting method. *Energies* 15 (2), 663. doi:10.3390/en15020663
- Deb, S., Tammi, K., Kalita, K., and Mahanta, P. (2018). Impact of electric vehicle charging station load on distribution network. *Energies* 11 (1), 178. doi:10.3390/en11010178
- Deng, M., Liu, Y., Hong, Y., Sun, Z., and Hao, J. (2024). Study on the grid supporting effects for GFM energy storage system in distribution networks under grid faults. *Energy Rep.* 12, 5801–5813. doi:10.1016/j.egyrs.2024.11.063
- Gangil, G., Goyal, S. K., and Saraswat, A. (2024). A multi-objective techno-economic operation of distribution network considering reactive power support from renewable energy and battery storage system. *J. Energy Storage* 102, 114116. doi:10.1016/j.est.2024.114116
- He, F., Zhou, J., Feng, Z. K., Liu, G., and Yang, Y. (2019). A hybrid short-term load forecasting model based on variational mode decomposition and long short-term memory networks considering relevant factors with Bayesian optimization algorithm. *Appl. Energy* 237, 103–116. doi:10.1016/j.apenergy.2019.01.055
- Hu, W., Yang, F., Shen, Y., Yang, Z., and Lei, Y. (2023). Dynamic risk assessment of voltage violation in distribution networks with distributed generation. *Entropy* 25 (12), 1662. doi:10.3390/e25121662
- Huang, X., Wu, D., and Boulet, B. (2023). Metaprobformer for charging load probabilistic forecasting of electric vehicle charging stations. *IEEE Trans. Intelligent Transp. Syst.* 24 (10), 10445–10455. doi:10.1109/tits.2023.3276947
- Ji, G., Yuan, Y., Fan, X., Yuan, R., and Li, X. (2020). Risk assessment of voltage limit violation on distribution network based on Cornish-Fisher expansion. *Acta Energetica Solaris Sin.* 41 (1), 358–366. doi:10.19912/j.0254-0096.2020.01.050
- Li, J., Zhang, L., Zhang, B., and Tang, W. (2023). Coordinated planning for flexible interconnection and energy storage system in low-voltage distribution networks to improve the accommodation capacity of photovoltaic. *Glob. Energy Interconnection-China* 6 (6), 700–713. doi:10.1016/j.gloi.2023.11.004
- Li, Y., Sun, N., Wang, D., Guo, F., and Li, F. (2024). A dynamic fault recovery strategy for an AC/DC distribution network with distributed energy storage system. *Power Syst. Prot. Control* 52 (18), 179–187. doi:10.19783/j.cnki.pspc.231547
- Lin, C., Bie, Z., and Chen, C. (2023). Operational probabilistic power flow analysis for hybrid AC-DC interconnected power systems with high penetration of offshore wind energy. *IEEE Trans. Power Syst.* 38 (4), 3016–3028. doi:10.1109/tpwrs.2022.3204707
- Liu, Z., Wang, Y., Vaidya, S., Ruehle, F., and Tegmark, M. (2025). KAN: kolmogorov-arnold networks. *arXiv*.
- Liu, M., Wang, J., Deng, S., Zhong, C., and Wang, Y. (2025). Short-term load probabilistic forecasting based on non-equidistant monotone composite quantile regression and improved MICN. *Energy* 320, 135339. doi:10.1016/j.energy.2025.135339
- Momani, M. A., Tashtush, S. A., Shahrour, R. J., and Alsatari, A. M. (2024). Modeling of long-term load forecast in Jordan based on statistical techniques. *J. Electr. Comput. Eng.* 2024, 8255513. doi:10.1155/2024/8255513
- Murali, S., Saini, P., Abhinav, K., Shankar, R., and Parida, S. K. (2024). Improved LSTM-based load forecasting embedded 3DOF (FOPI)-FOPD controller for proactive frequency regulation in power system. *IEEE Trans. Industry Appl.* 60 (6), 8213–8227. doi:10.1109/tia.2024.3443243
- Prakash, K., Ali, M., Siddique, M. N. I., Karmaker, A. K., Pota, H. R., Dong, D., et al. (2022). Bi-level planning and scheduling of electric vehicle charging stations for peak shaving and congestion management in low voltage distribution networks. *Comput. & Electr. Eng.* 102, 108235. doi:10.1016/j.compeleceng.2022.108235
- Ryu, S., and Yu, Y. (2024). Quantile-mixer: a novel deep learning approach for probabilistic short-term load forecasting. *IEEE Trans. Smart Grid* 15 (2), 2237–2250. doi:10.1109/tsg.2023.3290180
- Salinas, D., Flunkert, V., Gasthaus, J., and Januschowski, T. (2020). DeepAR: probabilistic forecasting with autoregressive recurrent networks. *Int. J. Forecast.* 36 (3), 1181–1191. doi:10.1016/j.ijforecast.2019.07.001
- Su, X., Zhang, C., Fu, Y., Li, Z., and Mi, Y. (2023). Two-stage optimal placement of BESS in an unbalanced active distribution network considering multi-scenario operation. *Power Syst. Prot. Control* 51 (10), 88–97. doi:10.19783/j.cnki.pspc.221514
- Villanueva, D., Feijóo, A. E., and Pazos, J. L. (2014). An analytical method to solve the probabilistic load flow considering load demand correlation using the DC load flow. *Electr. Power Syst. Res.* 110, 1–8. doi:10.1016/j.epsr.2014.01.003
- Wan, A., Chang, Q., Al-Bukhaiti, K., and He, J. (2023). Short-term power load forecasting for combined heat and power using CNN-LSTM enhanced by attention mechanism. *Energy* 282, 128274. doi:10.1016/j.energy.2023.128274
- Wang, Q., Tang, J., Li, F., Huang, W., and Xie, K. (2024). Reliability assessment of active distribution network considering aging effects of multiple devices. *Adv. Technol. Electr. Eng. Energy* 43 (7), 102–112. doi:10.12067/ATEEE2211024
- Xu, C., and Chen, G. (2024). Interpretable transformer-based model for probabilistic short-term forecasting of residential net load. *Int. J. Electr. Power Energy Syst.* 155, 109515. doi:10.1016/j.ijepes.2023.109515
- Yu, J., Li, Q., Du, Y., Wang, R., and Guo, D. (2024). Voltage over-limit risk assessment of wind power and photovoltaic access distribution system based on day-night segmentation and Gaussian mixture model. *Energy Rep.* 12, 2812–2823. doi:10.1016/j.egyrs.2024.08.079
- Zheng, G., Lei, X., Wang, X., and Luo, X. (2020). Earthquake simulation and risk assessment of distribution network. *Trans. China Electrotech. Soc.* 35 (24), 5218–5226. doi:10.19595/j.cnki.1000-6753.tces.191495
- Zhou, G., Bo, R., Chien, L., Zhang, X., and Su, D. (2018). GPU-accelerated algorithm for online probabilistic power flow. *IEEE Trans. Power Syst.* 33 (1), 1132–1135. doi:10.1109/tpwrs.2017.2756339
- Zhu, Z., Liang, L., Lei, S., Zheng, R., and Gryazina, E. (2025). An optimization model for identifying backbone networks to enhance the resilience of distribution networks. *Int. J. Electr. Power & Energy Syst.* 170, 110839. doi:10.1016/j.ijepes.2025.110839